

PAPER • OPEN ACCESS

Impact of error fields and error field correction on heat fluxes in SPARC

To cite this article: S. Munaretto *et al* 2025 *Nucl. Fusion* **65** 046007

View the [article online](#) for updates and enhancements.

You may also like

- [Error field predictability and consequences for ITER](#)
M. Pharr, N.C. Logan, C. Paz-Soldan et al.
- [Implications of vertical stability control on the SPARC tokamak](#)
A.O. Nelson, D.T. Garnier, D.J. Battaglia et al.
- [Design of passive and structural conductors for tokamaks using thin-wall eddy current modeling](#)
A.F. Battey, C. Hansen, D. Garnier et al.

Impact of error fields and error field correction on heat fluxes in SPARC

S. Munaretto^{1,*} , A. Kleiner¹ , R.M. Churchill¹ , D. Corona¹ , T. Looby² , M. Scotto d'Abusco¹  and A. Wingen³ 

¹ Princeton Plasma Physics Laboratory, 100 Stellarator Rd, Princeton, NJ 08540, United States of America

² Commonwealth Fusion Systems, Devens, MA, United States of America

³ Oak Ridge National Laboratory, Oak Ridge, TN, United States of America

E-mail: smunaret@pppl.gov

Received 20 December 2024, revised 7 February 2025

Accepted for publication 24 February 2025

Published 5 March 2025



Abstract

Using a single toroidal array of coils to reduce the $m, n = 2, 1$ resonant error field (EF) produced by the misalignment of the axisymmetric coils in SPARC can result in the enhancement of the local divertor heat fluxes. Managing high divertor heat fluxes ($q_{\parallel} \simeq 10 \text{ GW m}^{-2}$) poses a challenge for compact tokamak devices such as SPARC. The presence of non-axisymmetric magnetic field perturbations adds complexity to the problem by generating intricate 3D edge magnetic topologies that alter the heat flux distributions on the target plates. The aim of this work is to investigate the impact of the EF correction (EFC) on the heat fluxes at the divertor plates in SPARC. The MHD code M3DC1 has been used to simulate the 3D magnetic perturbations generated by the shift and tilt of several axisymmetric coils within specified tolerances, as well as from the array of EFC coils located at the midplane. Using a heuristic model that extends the concept of an axisymmetric heat flux layer to 3D plasmas, the resultant heat flux distributions is derived from magnetic footprints calculated with the MAFOT code. The results show that the EFC could either decrease or further enhance the local heat flux when used to correct the $m, n = 2, 1$ resonant EF to enhance the core plasma performance.

Keywords: MHD, plasma response, 3D fields, SPARC, heat fluxes, footprints

(Some figures may appear in colour only in the online journal)

1. Introduction

The presence of non-axisymmetric magnetic fields—also known as 3D fields or error fields (EFs)—is unavoidable in tokamak operation. These 3D fields can arise from, for example, engineering tolerances, thermal stresses, coil feeders, small mechanical vibrations, discrete coil number, etc.

Although they are several orders of magnitude smaller than the axisymmetric field ($\delta b/B \simeq 10^{-4}$) they have deleterious effects on plasma performance, including mode locking [1, 2], rotation braking from neoclassical toroidal viscosity [3, 4], and a reduction in thermal particle confinement (also known as ‘density pump out’) [5–8].

Another consequence of the presence of non-axisymmetric magnetic field perturbations is the formation of a stochastic edge layer that consists of a mixture of ergodic field lines (ergodic region) and extended flux tubes (laminar zone) that significantly alter the properties of the heat and particle flux distributions on the divertor target plates [9–13] and that might lead to a local enhancement of the heat fluxes [14, 15].

A common approach to improve plasma performances is the superposition of 3D fields generated by toroidal arrays of

* Author to whom any correspondence should be addressed.



Original Content from this work may be used under the terms of the [Creative Commons Attribution 4.0 licence](https://creativecommons.org/licenses/by/4.0/). Any further distribution of this work must maintain attribution to the author(s) and the title of the work, journal citation and DOI.

picture frame coils (dubbed 3D coils) to compensate for the EFs [16–21]. SPARC tokamak also plans on using 3D coils for EF correction (EFC) [22].

SPARC is a high-field ($B_0 = 12.2$ T), compact ($R_0 = 1.85$ m, $a = 0.57$ m) tokamak [23] under construction that is predicted to achieve peak unmitigated divertor parallel heat flux greater than 10 GW m^{-2} [24]. Such heat flux exceeds all material limits for melting by orders of magnitude and needs to be mitigated to about $10\text{--}20 \text{ MW m}^{-2}$ by a combination of radiative losses, expansion of wetted areas, change in incident angle, and dynamic strike point sweeping. Given the great challenge heat fluxes pose to the machine operation, it is important to investigate all possible aspects that can impact them. The main aim of this work is to investigate the impact of EFC on the heat fluxes at the divertor plates in SPARC.

Section 2 contains a description of the codes used for this study and an explanation of the choices made. In section 3 the results obtained are presented and discussed. Section 4 summarizes the findings and their implications for SPARC.

2. Methodology

A representative equilibrium of the SPARC tokamak was chosen as baseline to perform this study. A poloidal cross section of the flux surfaces is shown in figure 1 together with the pressure and the safety factor (q) radial profiles. The equilibrium is double null and upside-down symmetric. The plasma current is $I_p = 8.7$ MA and the toroidal field on the magnetic axis is $B_T = 12.2$ T. The size and location of the axisymmetric coils (also called 2D coils) are shown by rectangles in panel (a), while the vertical extension of the 3D coils (also called EFC coils, or EFCCs) are shown by solid lines with a dot at the extremities. The coils considered in this study are highlighted in orange, and their abbreviated name is printed next to them.

2.1. 3D perturbation and plasma response

To calculate the perturbation of the axisymmetric magnetic field due to the 3D field and the plasma response to it, the resistive MHD code M3D-C1 [25, 26] has been used. A single fluid model with no rotation and Spitzer resistivity was adopted. More details on how the linear plasma response to non-axisymmetric fields is calculated in M3D-C1 can be found in [27].

The perturbation due to misalignment of axisymmetric coils is calculated as an $n = 1$ perturbation (with n denoting the toroidal periodicity) produced by a shift or a tilt of such coil, using the model presented in detail in [28]. For each 2D coil outside of the center stack (i.e. those in orange in figure 1), an M3D-C1 simulation of a 1 mm shift and 1 mrad tilt is run. The current of each 2D coil is that needed to obtain the equilibrium shown in figure 1. Since not all the coils are energized in the considered equilibrium, a current of 1 kA-turn is associated with the 2D coils that have no current to preserve the equilibrium while still producing a 3D perturbation.

These values of current will be used for the rest of the manuscript. Figure 2 on the left outlines a typical shift and tilt of the 2D coils, and on the right shows the radial profile of the perturbed magnetic field normal to the flux surfaces (δb_n) caused by their respective misalignment. In plots (b) and (c), the solid and dashed lines correspond to the misalignment of the PF2U and PF2L coils respectively and the shaded regions correspond to a variation of 10% of the calculated value. It is important to note that the δb_n radial profiles agree (within 10%) for the upper and lower coil respectively, as expected due to the up-down symmetric nature of the configuration, suggesting that the computational grid used is adequate to avoid non-physical results.

2.2. Magnetic footprints

The presence of 3D fields causes field lines that would otherwise have been confined within the unperturbed last closed flux surface (LCFS) to intersect the plasma facing components (PFCs) through the formation of the so-called stable and unstable manifolds [9, 29, 30]. In this work, the MAFOT code [11] is used to trace field lines from the target region toward the plasma. A field line is followed until it hits another PFC or until it is followed for a number of steps that exceed a user defined threshold. For each field line, both the minimum unperturbed ψ_N (normalized poloidal flux) and the length of the field line (L_c , the so-called connection length) are recorded. An example of a magnetic footprint is shown in figure 3(b). The vertical axis is the distance along the wall from the high-field side midplane (dubbed Swall), and the horizontal axis is the toroidal angle (ϕ). The colors correspond to the minimum ψ_N (ψ_{\min}) reached by a field line launched from that element of the grid. The white region represents the field lines that stay in the scrape off layer (SOL) or in the private flux region (PFR). The distinction between field lines that are in the SOL or in the PFR and the field lines that would have been closed if there were no 3D fields, called lobes, is done based on the connection length. For a field line to be considered part of a lobe it needs to complete a full poloidal turn. Figure 3(a) illustrates that there is a clear separation in L_c between the lobes and the other field lines. Here, the y axis is the ψ_{\min} of a field line and the x -axis its connection length. A clear gap is evident at about $L_c \simeq 0.1$ km in this example. On the left of this gap there are two groups of field lines: one with large ψ_{\min} that represent the SOL field lines; and one with small ψ_{\min} representing the PFR. On the right of the gap are the field lines that are part of the lobes.

In SPARC, 3D fields can be generated either by a toroidal array of EFCCs or by the misalignment of the 2D coils. The following 2 sections will illustrate the magnetic footprints generated by each of these mechanisms.

2.3. Magnetic footprints generated by 3D coils

In figure 1(a) the poloidal location of the EFCCs is illustrated. Although all of them can produce 3D fields, in this work only the array at the midplane is considered, the EFCC Midplane (EFCCM) array. It is the one shown in orange in

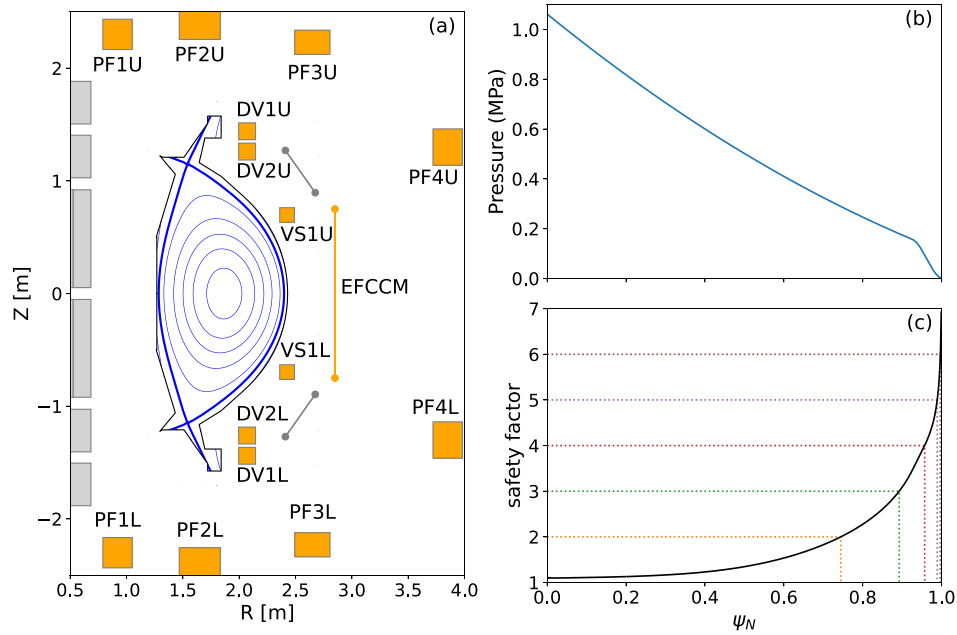


Figure 1. (a) Schematic of the poloidal cross section of the SPARC tokamak. The squares represent the position of the axisymmetric coils, the lines with a dot at the extremities the 3D coils. The coils in orange are those considered for the error field study. These have their abbreviated name next to them, where PF stand for *poloidal field*, DV stands for *divertor*, VS for *vertical stability*, EFCC for *error field correction coil*, and U, M and L for *upper, midplane and lower* respectively. The flux surfaces of the considered equilibrium are given in blue. (b) Shows the radial profile of the pressure and (c) the radial profile of the safety factor q with the location of several $n = 1$ rational surfaces highlighted.

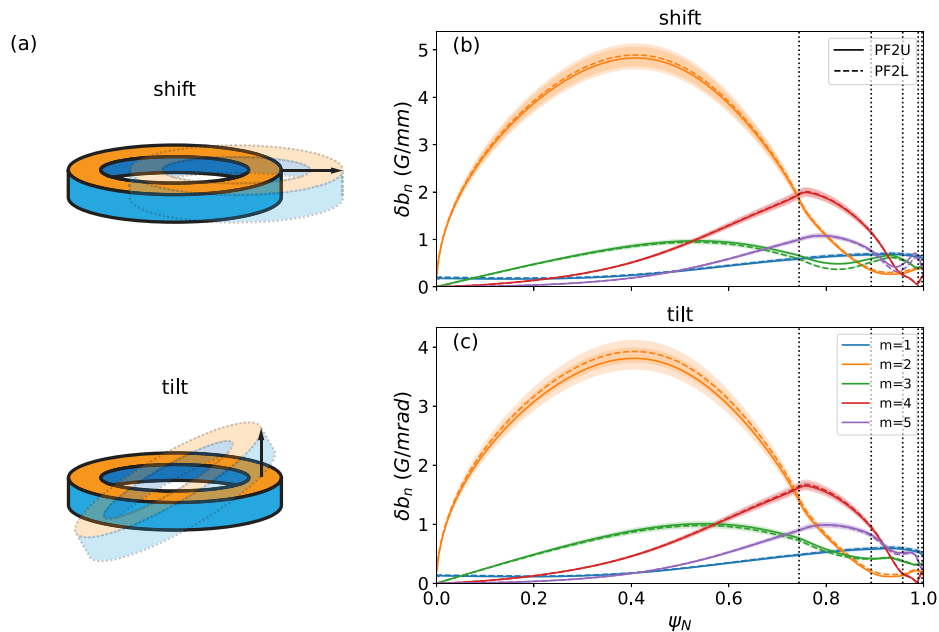


Figure 2. (a) Schematic of a shift, on top, and a tilt, on bottom, of an axisymmetric coil. (b) and (c) radial profile of the perturbed magnetic field normal to the flux surfaces for the shift (b) and tilt (c) of the PF2U coil (solid lines) and for the PF2L coil (dashed lines). The different colors represent the different poloidal components (m), from $m = 1$ to $m = 5$.

the figure 1(a). The EFCCM array is composed of six toroidally spread picture frame coils with a major radius $R = 2.93$ m, each coil with a toroidal extension of approximately $l = 2$ m and a vertical extension of approximately $h = 1.5$ m. The

maximum amount of current that can be driven through these coils is $I_{\text{COIL}} = 160$ kAt, which corresponds to the possibility of generating a $n = 1$ field with a maximum amplitude of about $I_{n=1} \simeq 103$ kAt.

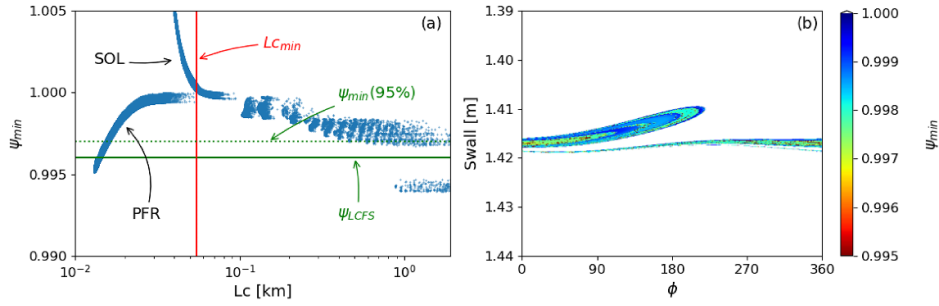


Figure 3. (a) Minimum unperturbed ψ_N reached by each traced field line as function of its connection length. (b) Magnetic footprint where the color represent the minimum unperturbed ψ_N reached by each traced field line as a function of the starting location. In white the field lines that have $L_c < 0.1$ km.

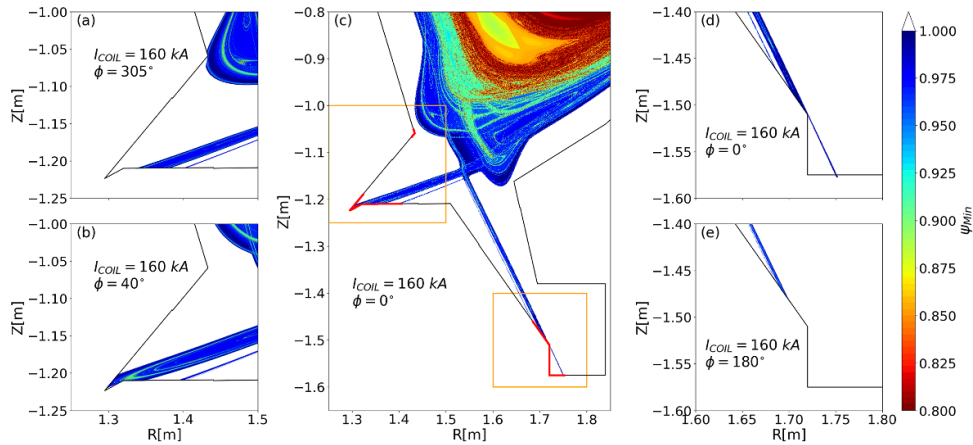


Figure 4. Series of laminar plots of field lines crossing a poloidal cross section, with the color representing the minimum ψ_N reached by each field line. Panel (c) shows an overview of the lower divertor region at $\phi = 0^\circ$, and the orange rectangles show the areas that are highlighted in the other four panels. (a) and (b) are the inner part of the divertor at $\phi = 305^\circ$ and $\phi = 40^\circ$ respectively. (d) and (e) are the outer part of the divertor at $\phi = 0^\circ$ and $\phi = 180^\circ$ respectively.

Figure 4 shows the impact that applying an $n = 1$ perturbation with the EFCCM at maximum amplitude has on the magnetic field lines in the lower divertor region. Panel (c) shows an overview of the lower divertor, with in black the axisymmetric approximation of the SPARC wall and the colors correspond to the ψ_{\min} reached by the field lines in that region, for a snapshot at the toroidal location of $\phi = 0^\circ$. Panels (a) and (b) show the same laminar plot only for the inner divertor region at two different toroidal locations, $\phi = 305^\circ$ and $\phi = 40^\circ$, respectively. At $\phi = 305^\circ$ there are field lines from within the unperturbed separatrix that intersect the corner region at $Z \simeq -1.05$ m while at $\phi = 40^\circ$ this does not happen, but there are field lines from within the unperturbed separatrix that reach further from the inner strike point (ISP) location up to the more vertical part of the inner divertor. Panels (d) and (e) show a zoom in of the outer divertor region at $\phi = 0^\circ$ and $\phi = 180^\circ$, respectively. It is possible to see that in panel (d) there are field lines from within the unperturbed separatrix that can extend beyond the diagonal divertor target and spill onto the horizontal X-target chamber floor. At $\phi = 180^\circ$ all the field lines are closer to the outer strike point (OSP). For the equilibrium considered, there are no field lines from within the unperturbed separatrix that can reach the outer corner (at about $Z \simeq -1.15$ m).

Figure 5 shows the magnetic footprints generated in the three regions where the field lines from within the unperturbed separatrix can reach the PFCs. The lower divertor is shown on the left and the upper one on the right. Panels (a) and (b) show that the inner corners are impacted only on a small toroidal angle, as well as the vertical part of the inner divertor (panels (c) and (d)) and the outer horizontal part (panels (e) and (f)). It is also important to observe that the magnetic footprints are upside-down symmetric with the exception of a toroidal shift. For the main strike points, the $\simeq 180^\circ$ shift is believed to be due to the $n = 1$ nature of the applied perturbation, while for the inner corner, the poloidal periodicity m is thought to also play a role.

2.4. Magnetic footprints generated by the misalignment of a 2D coil

Due to the linearity of the plasma response calculation, the shift and tilt calculation performed with M3D-C1 can be easily scaled to the desired misalignment. Since the tolerance set for the considered 2D coils is 2.5 mm, the shift of a 2D coil can be scaled directly by a factor of 2.5, while the scaling factor of the tilt depends on the major radius of the coil considered.

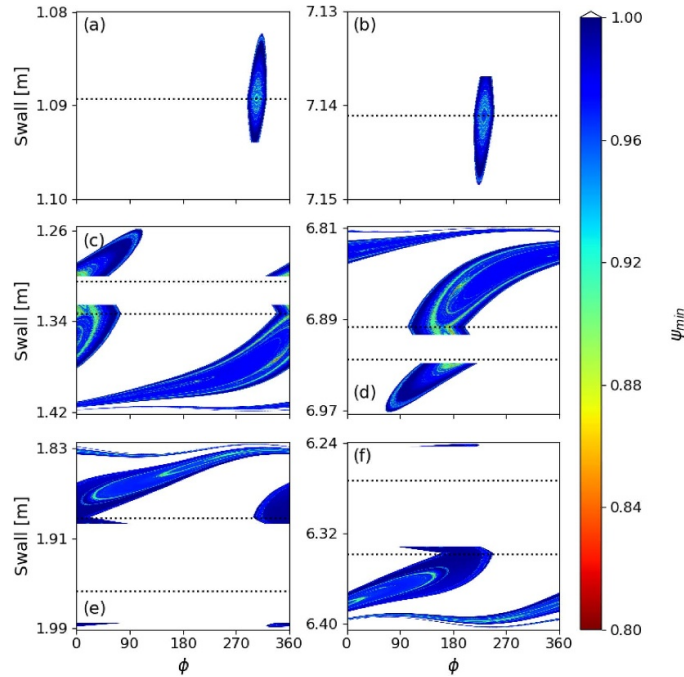


Figure 5. Magnetic footprints generated by the EFCCM coils with a $n = 1$ periodicity and $I_{\text{COIL}} = 160$ kA at on different locations of the SPARC wall. (a), (c) and (e) are located in the lower portion of the machine, while (b), (d) and (f) in the upper portion. The *Swall* locations of (a), (b) and (c) are highlighted in red in figure 4(c).

Figures 6(a) and (c) show the magnetic footprints generated by the shift of the PF4L coil (see figure 1) on the inner and outer divertor plate, respectively, while figures 6(b) and (d) show the magnetic footprints generated by the tilt of the same coil. It is possible to see that in this case the extension on the wall of the footprint does not exceed 2 mm.

It is not highly probable that a coil has only a shift or a tilt, but most likely there will be a combination of the two. Figures 6(e) and (f) show the magnetic footprint resulting from a combination of shift and tilt of the PF4L coil by 2.5 mm each with relative phase $\Delta\phi = \phi_{\text{tilt}} - \phi_{\text{shift}} = 0^\circ$ and $\Delta\phi = 180^\circ$, respectively. It is clear that the relative phase between the two perturbations plays an important role in determining the size of the magnetic footprint, as expected [31, 32].

2.5. Creating an EFs database

There are infinite ways to combine the shifts and the tilts of the 2D coils in SPARC, therefore about one thousand possible combinations have been randomly selected for this study. Three main constraints were applied:

- (i) each coil is shifted and tilted by its maximum allowed misalignment in order to fix the amplitude;
- (ii) the phase of the PF1U shift is fixed to $\phi = 0^\circ$ in order to focus only on the relative phase and neglect the absolute phase given the toroidal symmetry of the considered PFCs;
- (iii) each shift is a multiple of 15° in order to consider only meaningful variations.

The EFC approach used in this study aims at full cancellation of the $2/1$ resonant field harmonic on the $q = 2$

surface [18]. For each case, the 3D field produced by the EFCCM coils is superimposed and its amplitude and phase are scanned, using the $n = 1$ resonant magnetic field at the $q = 2$ surface ($\delta b_{n,\text{RES}}(q = 2)$) as figure of merit. An example of the resonant field due to the misalignment of the 2D coils and its correction, as well as the variation of $\delta b_{n,\text{RES}}(q = 2)$ as a function of the amplitude and phase of the EFCCM coils, is shown in figure 7.

2.6. 3D heat fluxes

In this work a heuristic model that extends the concept of an axisymmetric heat flux layer to 3D plasmas is used to associate heat fluxes to the magnetic footprints. In this section a short recap of this model is given, while a detailed description of it can be found in [33]. In an axisymmetric plasma, the heat fluxes to the divertor (q) can be described by plasma quantities at the midplane using the so-called Eich profile [34]:

$$q(R(\psi_N)) = \frac{q_0}{2} \exp \left[\left(\frac{S}{2\lambda_q} \right)^2 - \frac{R - R_0}{\lambda_q} \right] \times \text{erfc} \left(\frac{S}{2\lambda_q} - \frac{R - R_0}{S} \right) + q_{\text{BG}}. \quad (1)$$

In equation (1), λ_q represents the width of the heat flux layer, S the spread of the PFR, $R(\psi_N)$ the major radius in the outer midplane as a function of the normalized poloidal flux, and R_0 the major radius on the low field side of the LCFS. As mentioned above, in the presence of 3D fields, the flux surface $\psi_N = 1$ is not the LCFS anymore. This is accounted for in the

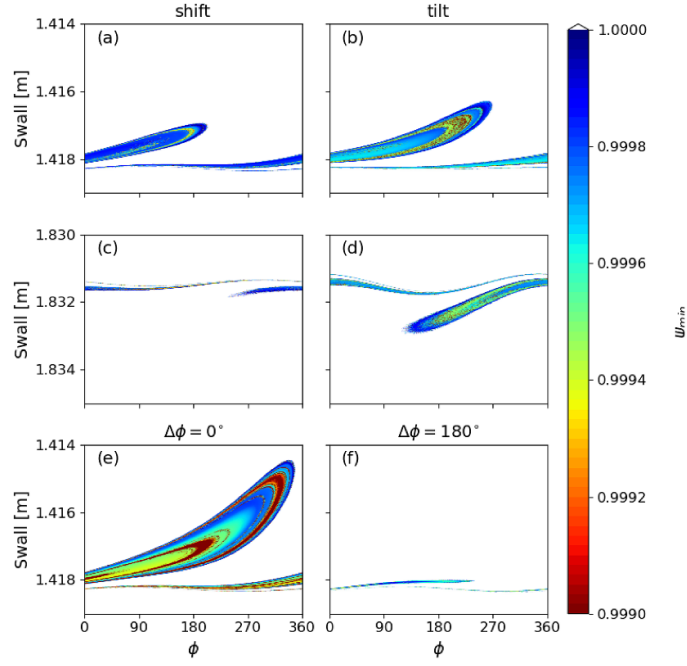


Figure 6. Magnetic footprints generated by the misalignment of the PF4L coil ($I_{PF4L} \simeq 4.3$ MA). (a) and (c) are magnetic footprints due to a 2.5 mm shift, (b) and (d) due to a 2.5 mrad tilt. (a) and (b) show the inner divertor region, (c) and (d) the outer one. Panels (e) and (f) show the magnetic footprints in the inner divertor region due to a combination of shift and tilt with even and odd parity respectively.

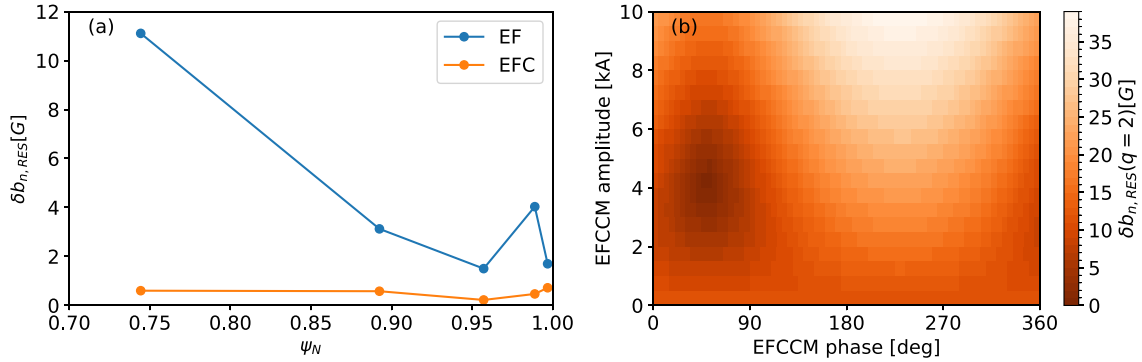


Figure 7. (a) Radial profile of the amplitude of the 3D fields at the $n = 1$ resonant surfaces for one of the combinations of coil misalignment. In blue due to the error field and in orange after the EFCM coil are deployed to minimize the $n = 1$ resonant magnetic field at the $q = 2$ surface. (b) Amplitude of $\delta b_{n,RES}(q = 2)$ for various combination of amplitude and phase of the $n = 1$ 3D fields produced by the EFCM.

following equation [33]:

$$q_{3D}(R(\psi_N)) = \begin{cases} q(R_0) & \psi_N < \psi_{LCFS}, L \geq L_{cmin} \\ q_s \frac{q(R)}{\max(q)} & \psi_N < 1, L < L_{cmin} \\ q(R) & \text{otherwise.} \end{cases} \quad (2)$$

In equations (1) and (2) there are four different parameters that determine the heat fluxes: L_{cmin} , ψ_{LCFS} , λ_q and S . The first two are determined by the magnetic footprint. L_{cmin} is the connection length that separates field lines that stay in the PFR from the others with $\psi_N < 1$ (see vertical red line in figure 3). An approach similar to that used in section 2.2 to identify the lobes can be used to estimate ψ_{LCFS} . As can be seen in figure 3(a), a gap in ψ_{min} is present in the lobes. Such a gap represents a separation between field lines that are directly connected to

the PFC and those that are connected through tunneling [9, 30], and is therefore a good candidate to represent the LCFS in the presence of 3D fields. This gap is not always present, especially in the presence of small perturbations such as in the EF case. To overcome this issue, a purely statistical approach can be used instead. In this case, ψ_{LCFS} is the ψ_N where 95% of the field lines in the lobes are confined outside the LCFS. It is possible to see in the figure that the two approaches lead to a similar value of ψ_{LCFS} .

Conversely from L_{cmin} and ψ_{LCFS} , λ_q and S are usually calculated by fitting experimental data and therefore are unknown for SPARC. Several scaling laws have been proposed to estimate λ_q . In this paper, if not otherwise specified, $\lambda_q = 0.6$ mm, as predicted by the Eich scaling #9 [35], and $S = \lambda_q = 0.6$ mm. An example of 3D heat fluxes is shown in figure 8. The magnetic footprint considered here is that of figure 3. The q_0 is

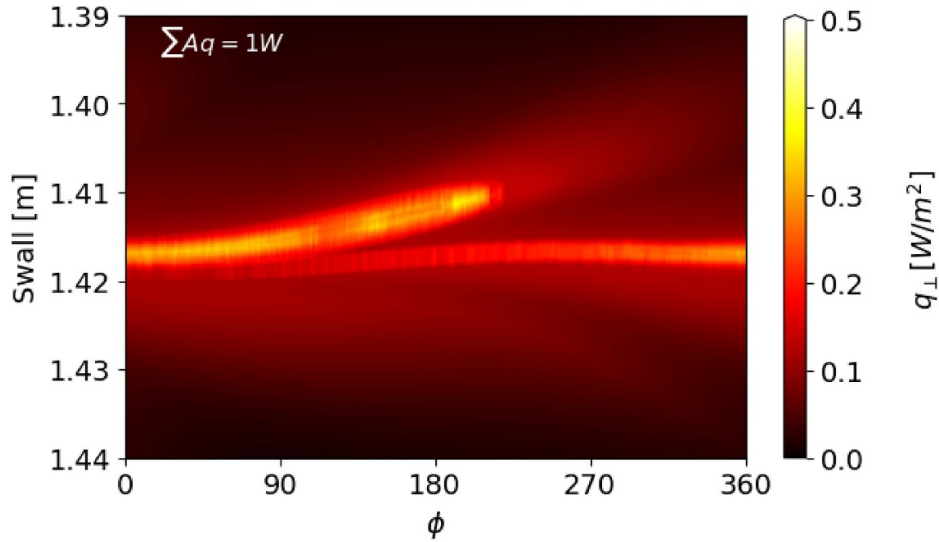


Figure 8. 3D heat flux distribution as a consequence of the magnetic footprint of figure 3. The total power on the plotted area is assumed to be 1 W, $\lambda_q = 0.6$ and $S = 0.6$.

calculated so that the total power over the area shown is 1 W. This is valid for all the heat flux calculations in this manuscript, so that the focus remains on the changes in the heat flux distribution.

3. Results and discussion

The results from the database of EFs described in section 2.5 are plotted in figure 9. In panel (a), each of the dots represents the peak heat flux of a case, in the x -axis when only the 2D coils misalignment is considered, and in the y -axis when the EFC is added. In panel (b), the x -axis is the case number and the y -axis is the change in peak heat flux when the EFC is included. The red star in panel (a) represents the peak heat flux in the axisymmetric case (no EF).

There are a few considerations that can be made from these results. First of all, as expected [14, 15], the presence of 3D fields, whether this is due to EFs or when EFC is included, increases the local peak heat flux. For the equilibrium considered, the increase can be up to a factor of 4. The second main consideration is that the application of EFC does not always decrease the peak heat flux. Among all the cases considered, about half of them saw a reduction in the peak heat flux after the application of the EFC. In a handful of cases the EFC resulted in an increase of the peak heat flux of more than 100% of the EF peak heat flux. The third consideration is that the range of possible peak heat flux is unchanged regardless of whether the EFC is considered or not. Moreover, in more than 70% of the cases, the variation in the peak heat flux after the EFC is applied, defined as $\Delta q_{\perp} = \frac{q_{\perp, \text{EFC}} - q_{\perp, \text{EF}}}{q_{\perp, \text{EF}}}$, is less than 25%. These results are explained by the fact that the EFC aims at minimizing the core resonant field, but such field is not correlated with the magnetic footprints, or at least it is not the main component that influences them [32]. At the same time, the 3D fields used for the EFC have similar amplitude to that of the EF themselves, so comparable 3D heat fluxes have to be expected.

To better understand what differentiates the various cases examined, four of them are analyzed in more details. Those cases are shown by magenta dots in figure 9(a), and the correspondent 3D heat fluxes are shown in figure 10. The left column show the heat fluxes in presence of EFs, while the right column shows how they change when the EFCCs are applied. (a) and (b) show the case marked as 1 in figure 9(a), where the peak heat flux with EF is about $\max(q_{\perp, \text{EF}}) \simeq 0.11 \text{ W m}^{-2}$ and increases by about 0.3% with EFC. (c) and (d) show the case marked as 2, where the peak heat flux with EF is about $\max(q_{\perp, \text{EF}}) \simeq 0.4 \text{ W m}^{-2}$ and with EFC it decreases by about 3%. (e) and (f) are the case marked as 3, where the EFC decreases the peak heat flux from $\max(q_{\perp, \text{EF}}) \simeq 0.23 \text{ W m}^{-2}$ to $\max(q_{\perp, \text{EF}}) \simeq 0.12 \text{ W m}^{-2}$, while (g) and (h) show the case number 4, where the EFC increases the peak heat flux from $\max(q_{\perp, \text{EF}}) \simeq 0.12 \text{ W m}^{-2}$ to $\max(q_{\perp, \text{EF}}) \simeq 0.25 \text{ W m}^{-2}$.

In figure 11 three quantities are plotted for each case in order to look for a relation between the predicted peak heat flux and magnetic field related properties. The left column shows the radial profile of the $n = 1$ resonant magnetic field, the center column shows the corresponding island width and the last column shows the distribution of ψ_{\min} . In blue the cases with only 2D coils misalignment and in orange the cases where the EFC is applied. The order of the rows is the same as that in figure 10. When considering $\delta b_{n=1, \text{RES}}$, it is possible to observe that in three of the four cases shown, the EFC reduces it at all the rational surfaces despite different impacts on the peak heat flux, suggesting a weak relation between the two quantities. A similar conclusion can be drawn looking at the island width. More interesting features are shown in the third column (ψ_{\min} distribution). Figures 11(c) and (f) show a similar range of ψ_{\min} with or without correction of the EF, with ψ_{\min} that can reach lower values in (f), in agreement with a larger peak heat flux. Figure 11(i) shows an extra group of field lines with ψ_{\min} around 0.995 that is removed when the correction coils are applied. This suggests that the penetration depth might play a role on the peak heat flux. Such hypothesis

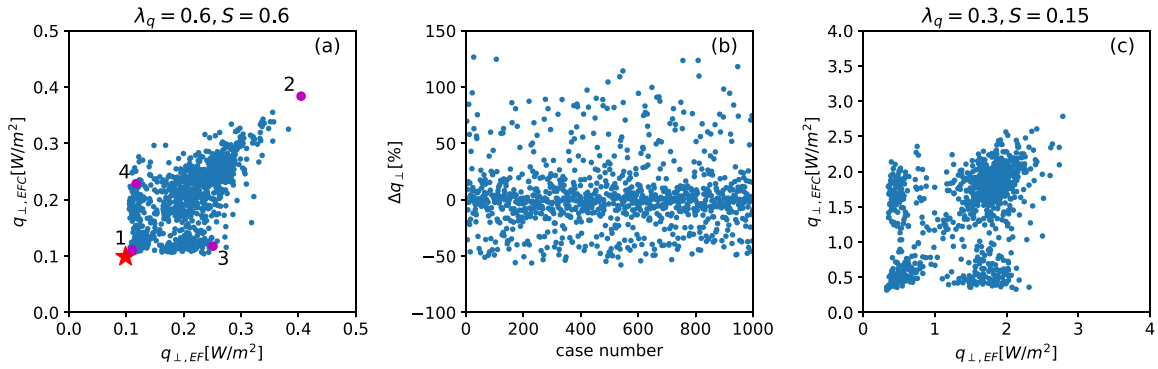


Figure 9. Peak heat flux resulting from the database of $n = 1$ error fields. (a) and (c) plot the peak heat flux with EFC versus peak heat flux without EFC. In (b) the variation in peak heat flux (Δq_{\perp}) for each of the considered case. In (a) and (b) $\lambda_q = 0.6$ and $S = 0.6$, in (c) $\lambda_q = 0.3$ and $S = 0.15$. The power on the considered area is 1 W. The red star in (a) marks the axisymmetric case ($q_{\perp} \simeq 0.1 \text{ W m}^{-2}$), the magenta dots are the cases chosen for the plots in figures 10 and 11, and the numbers indicate the correspondent rows.

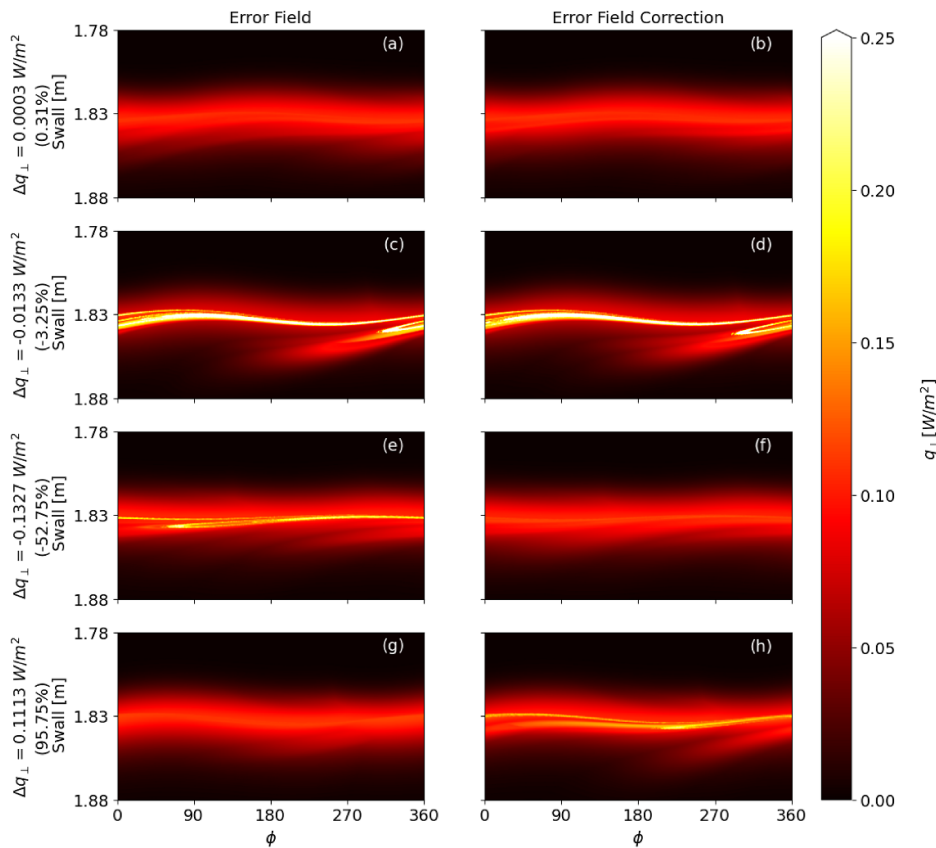


Figure 10. 3D heat fluxes for the cases highlighted in magenta in figure 9(a). On the left—(a), (c), (e) and (g)—the error field cases, on the right—(b), (d), (f) and (h)—the respective cases with the error field correction applied. All plots share the same linear color scale.

is confirmed by figure 11(l), where the group of field lines with ψ_{\min} around 0.994 is present only when the EFC is applied, and this corresponds to an increase of about 95% in the peak heat flux.

It is also important to observe that so far the focus has been on the OSP. A similar analysis done on the ISP brings overall comparable results, but OSP and ISP do not always show the same behavior for a given misalignment. An example is shown in figure 12 where the first row corresponds to the ISP, and the second row corresponds to the OSP. It is possible to see that

while the EFC changes the heat flux distribution in the ISP and decreases the peak heat flux magnitude by about 73%, in the OSP both the heat flux distribution and the peak heat flux magnitude are left almost unchanged. It is important to note that the power in both ISP and OSP is considered to be 1 W on the shown surface, but the area in the 2 cases is slightly different, so comparing the absolute values shown in the plots might be misleading.

Finally, a consideration on the choice of the transport parameters. As mentioned in section 2.6, λ_q is determined using

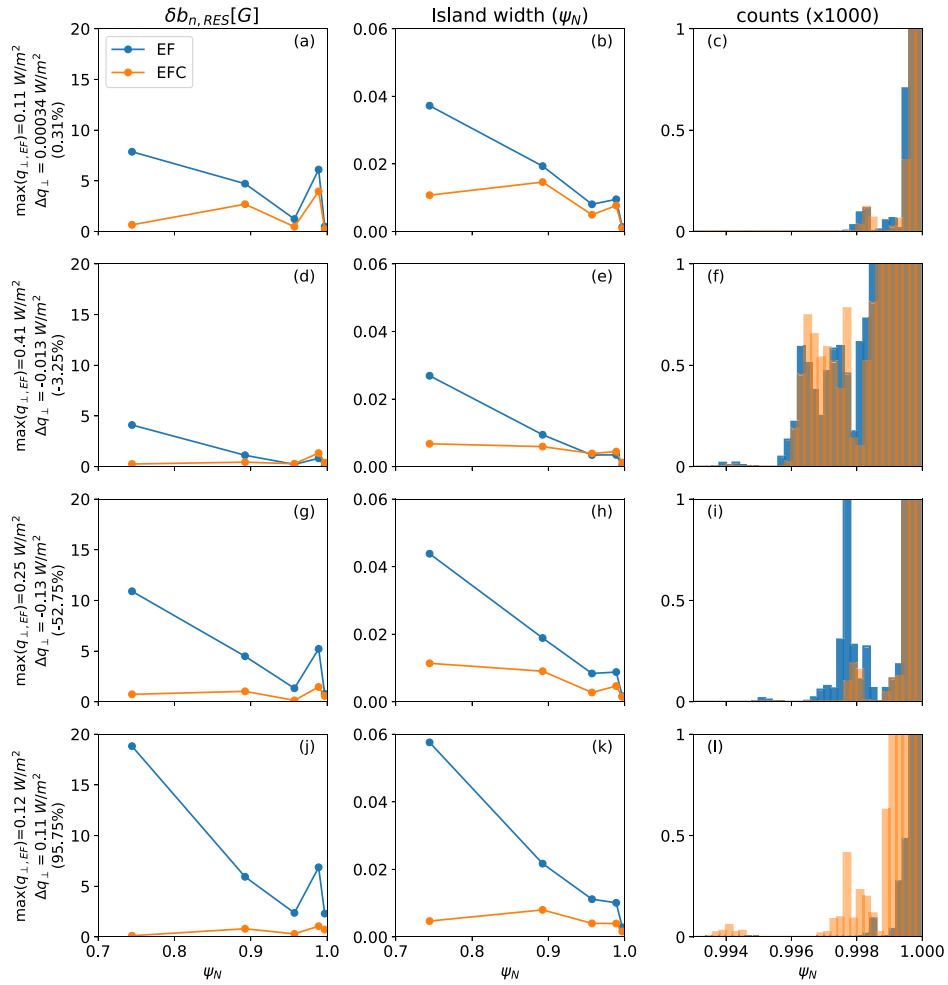


Figure 11. In (a), (d), (g) and (j) the radial profile of the $n = 1$ resonant magnetic field, in (b), (e), (h) and (k) the radial profile of the $n = 1$ island width at the resonant locations, and in (c), (f), (i) and (l) the histogram of the ψ_{\min} of the traced field lines. Each row corresponds to a different case, and the case are ordered as in figure 10. In blue when the EFC is not considered, and in orange when it is.

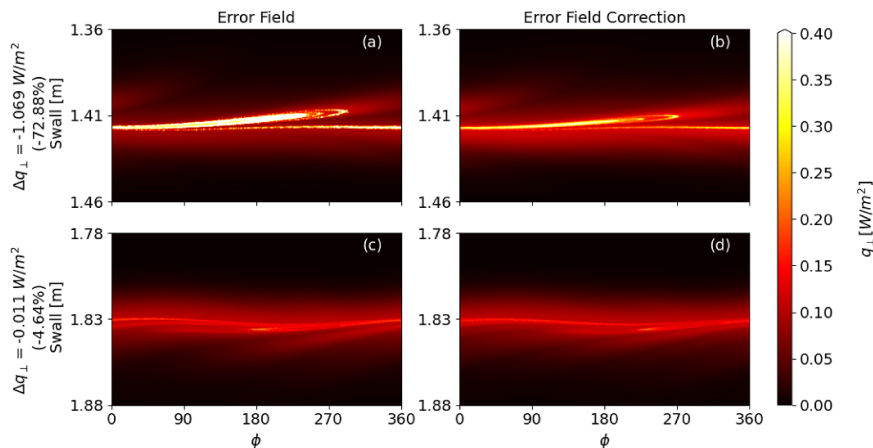


Figure 12. 3D heat fluxes in the ISP—(a) and (b)—and in the OSP—(c) and (d)—for a case in the database. On the left—(a) and (c)—when the EFC is not applied, and on the right—(b) and (d)—when it is.

scaling laws. A different option for λ_q in SPARC is given by the Eich scaling #15 [35], which predicts $\lambda_q = 0.3$ mm. Similarly, a more strict choice of S can be half of λ_q , $S = 0.15$ mm. The results for such choice for the overall picture are

shown in figure 9(c). Compared to the previous case, it is possible to observe that the qualitative results are similar, but the value of the peak heat fluxes increases by about an order of magnitude. This indicates that for such small magnetic field,

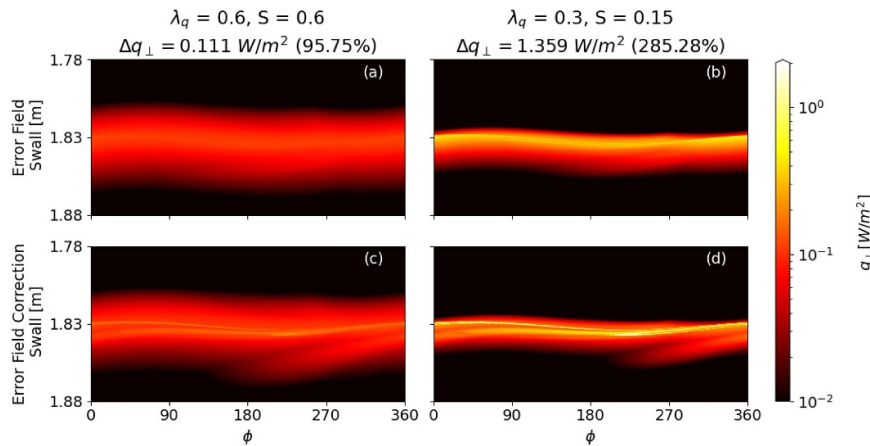


Figure 13. 3D heat fluxes for a case shown in figure 10. On the top—(a) and (b)—when the EFC is not applied, and on the bottom—(c) and (d)—when it is. On the left—(a) and (c)—when the transport coefficients are $\lambda_q = 0.6$ and $S = 0.6$, and on the right—(b) and (d)—when they are $\lambda_q = 0.3$ and $S = 0.15$. All plots share the same logarithmic color scale.

the transport still plays an important role in determining the heat flux profiles. An example of what this means is shown in figure 13. The plots in the top row correspond to a case with EF and the bottom row to the same case with EFC. The left column shows the same case of figures 10(g) and (h), while the right column has the heat fluxes computed with $\lambda_q = 0.3$ mm and $S = 0.15$ mm. To be noted that the color code in this figure is on a logarithmic scale. This figure highlights that small changes in 3D fields and in the choice of the transport coefficients can lead to very different heat flux patterns. This is due to the compact size of the SPARC device and the small amplitude of the 3D fields that make the difference between ψ_{LCFS} and $\psi_{\text{N}} = 1$ at the midplane being comparable to λ_q .

4. Conclusions

SPARC is expected to deal with parallel heat fluxes greater than 10 GW m^{-2} [24] to the divertor plates. The presence of 3D fields modifies the heat flux deposition, and an unavoidable source of non-axisymmetric fields are the EFs. The main goal of this work has been to investigate the impact of the $n = 1$ EFC done with the EFCCM array of coils on the heat fluxes at the divertor plates.

The main conclusion is that the use of the EFCCM to improve plasma performances does not correct for the local peak heat flux. On the contrary, it was observed that the EFC can decrease the peak heat flux by a factor of 2, but also increase it by more than a factor of 2 in other cases. This is expected since the EFC aims at minimizing the resonant field in the core, that was already observed to not be directly correlated to the magnetic footprints at the divertor [32]. This study also led to a few other interesting observations.

One is that the range of possible peak heat fluxes due to the $n = 1$ misalignment of the 2D coils is not modified by the application of the EFC, and this is related to the fact that the EFCCM amplitude is comparable to that of the EF. It was also shown that using the EFCCM at full current could lead to heat and particle fluxes in undesirable locations. Another

important observation is that an increase or decrease of the peak heat flux on the OSP does not always correspond to an increase/decrease on the ISP. A final observation is that in a compact size device, when small 3D perturbations are considered, transport still plays an important role on determining the SOL width.

This work was limited at studying the impact of the EFC using a single array of 3D coils, a fixed 2D equilibrium and toroidally symmetric PFC. Next steps will include: the use of the EFCCU and EFCCL arrays of 3D coils in order to control the poloidal spectrum of the applied correction field and investigate the possibility to minimize both the resonant field and the peak heat flux at the same time; investigating the impact of EFC on a range of possible equilibrium choices for SPARC; use the new features of the HEAT toolkit [36–39] to study the impact of the EFC on a more realistic 3D PFC.

Acknowledgments

This material is based upon work supported by the US Department of Energy, Office of Science, Office of Fusion Energy Sciences, under Awards DE-AC02-09CH11466 and DE-AC05-00OR22725. This work is supported in part by Commonwealth Fusion Systems. The United States Government retains a non-exclusive, paid-up, irrevocable, world-wide license to publish or reproduce the published form of this manuscript, or allow others to do so, for United States Government purposes. The data that supports the findings of this study are openly available at [40].

ORCID iDs

S. Munaretto <https://orcid.org/0000-0003-1465-0971>
A. Kleiner <https://orcid.org/0000-0002-5800-8027>
R.M. Churchill <https://orcid.org/0000-0001-5711-746X>
D. Corona <https://orcid.org/0000-0002-1291-1552>
T. Looby <https://orcid.org/0000-0002-1275-2758>

M. Scotto d'Abusco  <https://orcid.org/0009-0001-7424-9242>

A. Wingen  <https://orcid.org/0000-0001-8855-1349>

References

- [1] Nave M.F.F. and Wesson J.A. 1990 Mode locking in tokamaks *Nucl. Fusion* **30** 2575
- [2] Fitzpatrick R. 1993 Interaction of tearing modes with external structures in cylindrical geometry (plasma) *Nucl. Fusion* **33** 1049
- [3] Shaing K.C. 2003 Magnetohydrodynamic-activity-induced toroidal momentum dissipation in collisionless regimes in tokamaks *Phys. Plasmas* **10** 1443–8
- [4] Cole A.J., Hegna C.C. and Callen J.D. 2008 Neoclassical toroidal viscosity and error-field penetration in tokamaks *Phys. Plasmas* **15** 056102
- [5] Hender T.C. *et al* 1992 Effect of resonant magnetic perturbations on COMPASS-C tokamak discharges *Nucl. Fusion* **32** 2091
- [6] Evans T.E. *et al* 2004 Suppression of large edge-localized modes in high-confinement DIII-D plasmas with a stochastic magnetic boundary *Phys. Rev. Lett.* **92** 235003
- [7] Liang Y. *et al* 2007 Active control of Type-I edge-localized modes with $n = 1$ perturbation fields in the JET tokamak *Phys. Rev. Lett.* **98** 265004
- [8] Kirk A. *et al* (the MAST Team) 2010 Resonant magnetic perturbation experiments on MAST using external and internal coils for ELM control *Nucl. Fusion* **50** 034008
- [9] Evans T.E., Roeder R.K.W., Carter J.A., Rapoport B.I., Fenstermacher M.E. and Lasnier C.J. 2005 Experimental signatures of homoclinic tangles in poloidally diverted tokamaks *J. Phys.: Conf. Ser.* **7** 174
- [10] Schmitz O. *et al* 2008 Identification and analysis of transport domains in the stochastic boundary of TEXTOR-DED for different mode spectra *Nucl. Fusion* **48** 024009
- [11] Wingen A., Evans T.E. and Spatschek K.H. 2009 High resolution numerical studies of separatrix splitting due to non-axisymmetric perturbation in DIII-D *Nucl. Fusion* **49** 055027
- [12] Wingen A., Evans T.E. and Spatschek K.H. 2009 Footprint structures due to resonant magnetic perturbations in DIII-D *Phys. Plasmas* **16** 042504
- [13] In Y. *et al* (the 3D Physics Task Force in KSTAR) 2019 Tamed stability and transport using controlled non-axisymmetric fields in KSTAR *Nucl. Fusion* **59** 056009
- [14] In Y. *et al* (3D Physics Task Force in KSTAR) 2017 Enhanced understanding of non-axisymmetric intrinsic and controlled field impacts in tokamaks *Nucl. Fusion* **57** 116054
- [15] LIANG R. *et al* 2022 Study on divertor heat flux under $n = 3$ and $n = 4$ resonant magnetic perturbations using infrared thermography diagnostic in EAST *Plasma Sci. Technol.* **24** 105103
- [16] Park J.-K., Boozer A.H., Menard J.E. and Schaffer M.J. 2008 Error field correction in ITER *Nucl. Fusion* **48** 045006
- [17] Park J.-K., Schaffer M.J., La Haye R.J., Scoville T.J. and Menard J.E. 2011 Error field correction in DIII-D Ohmic plasmas with either handedness *Nucl. Fusion* **51** 023003
- [18] Yueqiang Liu A.K. and Thornton A.J. (the MAST Team) 2014 Modelling intrinsic error field correction experiments in MAST *Plasma Phys. Control. Fusion* **56** 104002
- [19] Kirk A., Yueqiang Liu Y., Martin R., Cunningham G. and Howell D. (the MAST Team) 2014 Measurement, correction and implications of the intrinsic error fields on MAST *Plasma Phys. Control. Fusion* **56** 104003
- [20] Paz-Soldan C., BATTERY R.J., Garofalo A.M., Hanson J.M., La Haye R.J., Lanctot M.J., Park J.K., Solomon W.M. and Strait E.J. 2014 The spectral basis of optimal error field correction on DIII-D *Nucl. Fusion* **54** 073013
- [21] Piron L. *et al* (JET Contributors, the EUROfusion Tokamak Exploitation Team, the ASDEX Upgrade Team and MAST-U Team) 2024 Error field detection and correction studies towards ITER operation *Nucl. Fusion* **64** 066029
- [22] Sweeney R. *et al* 2020 MHD stability and disruptions in the SPARC tokamak *J. Plasma Phys.* **86** 865860507
- [23] Creely A.J. *et al* 2020 Overview of the SPARC tokamak *J. Plasma Phys.* **86** 865860502
- [24] Kuang A.Q. *et al* 2020 Divertor heat flux challenge and mitigation in SPARC *J. Plasma Phys.* **86** 865860505
- [25] Jardin S.C., Ferraro N., Luo X., Chen J., Breslau J., Jansen K.E. and Shephard M.S. 2008 The M3D-C1 approach to simulating 3D 2-fluid magnetohydrodynamics in magnetic fusion experiments *J. Phys.: Conf. Ser.* **125** 012044
- [26] Breslau J., Ferraro N. and Jardin S. 2009 Some properties of the M3D-C1 form of the three-dimensional magnetohydrodynamics equations *Phys. Plasmas* **16** 092503
- [27] Ferraro N.M. 2012 Calculations of two-fluid linear response to non-axisymmetric fields in tokamaks *Phys. Plasmas* **19** 056105
- [28] Ferraro N.M., Park J.-K., Myers C.E., Brooks A., Gerhardt S.P., Menard J.E., Munaretto S. and Reinke M.L. 2019 Error field impact on mode locking and divertor heat flux in NSTX-U *Nucl. Fusion* **59** 086021
- [29] Evans T.E., Roeder R.K.W., Carter J.A. and Rapoport B.I. 2004 Homoclinic tangles, bifurcations and edge stochasticity in diverted tokamaks *Contrib. Plasma Phys.* **44** 235–40
- [30] Evans T.E. 2008 *Implications of Topological Complexity and Hamiltonian Chaos in the Edge Magnetic Field of Toroidal Fusion Plasmas* (World Scientific) pp 147–76
- [31] Munaretto S., Evans T.E., Ferraro N.M., Orlov D.M., Trevisan G.L. and Wu W. 2019 Assessment of equilibrium field coil misalignments on the divertor footprints in NSTX-U *Nucl. Fusion* **59** 076039
- [32] Munaretto S., Orlov D.M., Paz-Soldan C., Bykov I., Lasnier C.J., Lyons B.C. and Wang H. 2021 Controlling the size of non-axisymmetric magnetic footprints using resonant magnetic perturbations *Nucl. Fusion* **62** 026018
- [33] Wingen A., Orlov D., Evans T.E., Bykov I. and Wilks T.M. 2021 New heat flux model for non-axisymmetric divertor infrared structures *Nucl. Fusion* **61** 016018
- [34] Eich T., Sieglin B., Scarabosio A., Fundamenski W., Goldston R.J. and Herrmann A. 2011 Inter-ELM power decay length for JET and ASDEX Upgrade: measurement and comparison with heuristic drift-based model *Phys. Rev. Lett.* **107** 215001
- [35] Eich T. *et al* 2013 Scaling of the tokamak near the scrape-off layer H-mode power width and implications for ITER *Nucl. Fusion* **53** 093031
- [36] Looby T., Reinke M., Wingen A., Menard J., Gerhardt S., Gray T., Donovan D., Unterberg E., Klabacha J. and Messineo M. 2022 A software package for plasma-facing component analysis and design: the heat flux engineering analysis toolkit (heat) *Fusion Sci. Technol.* **78** 10–27
- [37] Wingen A., Scotto d'Abusco M., Churchill M., Corona D., Ferraro N., Kleiner A., Looby T. and Munaretto S. 2024 Development and validation of non-axisymmetric heat flux simulations with 3D fields using the heat code *Bull. Am. Phys. Soc.* (available at: <https://meetings.aps.org/Meeting/DPP24/Session/TO06.15>)

- [38] Scotto d'Abusco M., Wingen A., Looby T., Ferraro N., Kleiner A., Churchill M., Corona D. and Munaretto S. 2024 3D heat flux modelling of rotating error field correction applied to the SPARC tokamak with the heat code *Bull. Am. Phys. Soc.* (available at: <https://meetings.aps.org/Meeting/DPP24/Session/NP12.118>)
- [39] Corona D., Munaretto S., Churchill M., Scotto d'Abusco M., Looby T. and Wingen A. 2024 Shadow masks predictions in SPARC tokamak plasma-facing components using heat code and machine learning methods *Bull. Am. Phys. Soc.* (available at: <https://meetings.aps.org/Meeting/DPP24/Session/NP12.119>)
- [40] Munaretto S. 2024 *Data for 'Impact of error field and error field correction on heat fluxes in SPARC'* (Princeton Plasma Physics Laboratory, Princeton University) (<https://doi.org/10.34770/s1cc-xg79>)